Computational Fluid Dynamics JOURNAL vol.4. no.1 April 1995 (59–78)

NUMERICAL ANALYSIS OF TURBULENT STRUCTURE IN A RECTANGULAR DUCT WITH SAND RIDGES

Hitoshi SUGIYAMA† Mitsunobu AKIYAMA†
Kazunori YAMANAKA† Masaru HIRATA‡

Abstract

A numerical analysis has been performed for developing turbulent flow in a rectangular duct with sand ridges using algebraic Reynolds stress model and boundary fitted coordinate system. These sand ridges are formed on river beds as a result of transport of fine sand due to the secondary currents. The numerical simulation results were compared with available experimental data. It is commonly known that in a rectangular duct with smooth walls a pair of vortices is formed in each quadrant of the duct cross section. Contrary that, in the rectangular ducts with sand ridges, both of the present calculation and the previous experiments suggest formation of the secondary flows over the ridges. The present numerical analysis simulates the developing process of the secondary currents, and shows that the secondary flow over the ridges is stronger than the one in the corner region. The calculated normal and shear stresses are in reasonably good agreement with the available experimental data.

1. INTRODUCTION

It has been known from published experimental data that the turbulence-driven secondary motion exists in non-circular ducts, which was defined as the secondary flow of the second kind by Prandtl. This motion is not caused by the pressure gradient but due to the anisotropic turbulence. Although this secondary flow velocity is only of the order of two or three percent of the streamwise bulk velocity, its presence displaces considerably the streamlines toward the corners of the duct, and induces relatively high velocity field there. Furthermore, this secondary motion produces high wall shear stress along the corner. Owing to these characteristic features, the turbulent flows accompanied by this secondary flow have been attracting keen interests of many scientists and engineers in various fields, such as mechanical, nuclear, chemical and civil engineerings. Understanding of the secondary flows in a non-circular duct is indispensable for clarifying the effects of turbulent convective heat and mass transfer.

In civil engineering, many river engineers have been studying theoretically as well as experimentally characteristic features connected with the secondary flows. Vanoni [1] pointed out that the spanwise distribution of sediment concentration varies periodically in wide open

Presented at the 7th Numerical Fluid Dynamics Symposium on December 20 to 22, 1993
Received on January 26, 1994.

† Dept. of Mechanical Systems Engineering, Utsunomiya University;
Ishii-cho 2753, Utsunomiya 321, Japan
‡ Dept. of Mechanical Engineering;
Shibaura Institute of Technology; Fukasaku 307, Oomiya 330, Japan

channel, and inferred that this fact may be caused by cellular secondary currents. Matthes [2] envisaged that there exists strong upward current near the river bed and that it develops up to the free surface and then forms so-called "boil", which has been observed as a vortex-ring-like swollen water on the surface. Kinoshita [3] found by means of aerial stereoscopic survey of flooded rivers that a boil consists of a central, low-speed zone and surrounding, high-speed zone, which has a spanwise size of approximately twice of the flow depth. He suggested that there exist cellular secondary current in a straight river that has a pair of counter-rotating streamwise vortices with a diameter of about the flow depth. After the flood had gone, Culbertson [4] and Karcz [5] found that longitudinal ridges and troughs that are called "sand ridge" are formed periodically on the river bed. Investigations on such cellular secondary currents and the associated river bed formation are important topics in river engineering.

A notable feature of sand ridge is that the ridge surfaces are generally smoother than those of the troughs. Müller and Studerus [6] carried out a laboratory experiment using a 0.6 m wide and 25 m long laboratory flume, measuring all three components of the velocity vector, and reported that secondary flow vortices are induced by four longitudinal stripes attached on the bed as roughness. Nezu and Nakagawa [7] have investigated experimentally the turbulent structure of cellular secondary currents using longitudinal ridge in air conduit. Taking into consideration the interaction between secondary currents and bedform, they set longitudinal ridge elements onto both of the lower and upper bottoms of the conduit, which simulates the longitudinal ridges and troughs of the river bedform.

In numerical analysis of river engineering, Noat and Rodi [8] presented the calculated results of open channel flow with free surface based on algebraic Reynolds stress model. Calculation of Demuren and Rodi [9] were carried out for the fully developed turbulent flow in a 5:1 ratio rectangular channel with a roughened wall, which has been studied experimentally by Hinze [10]. Calculated results showed distortion of the primary velocity contours, distribution of the turbulent shear stress and the kinetic energy along the wall bisector. For turbulent flows in compound channels, numerical analyses have been presented by many researchers. On the other hand, calculations of three dimensional turbulent flows with sand ridges are very few. This is due to difficulty to set the boundary conditions along the complex figure. Furthermore, it is necessary to calculate using anisotropic turbulence model in order to predict precisely the secondary motions near the sand ridges.

The authors [11] have discussed the advantages and disadvantages of several typical Reynolds stress models and, based on these examinations, improved the pressure strain correlations of the Reynolds stress equations. This Reynolds stress model ha been applied for several kinds of turbulent flows in order to confirm the applicability of the Reynolds stress model [12], [13]. As mentioned above, very little numerical study has been reported concerning the secondary flow behavior and its generation mechanism in flows with sand ridges.

Therefore, the purpose of the present research is to analyze the developing turbulent flow in a rectangular duct with sand ridges using the modified Reynolds stress model coupled with $k-\varepsilon$ model. The numerical results are compared with the published experimental data that has been measured in detail by Nezu and Nakagawa [7]. In calculation, boundary-fitted coordinate system is adopted to treat the boundary condition precisely. It is hoped that the numerical simulation of three dimensional turbulent flows with sand ridges makes the developing mechanism

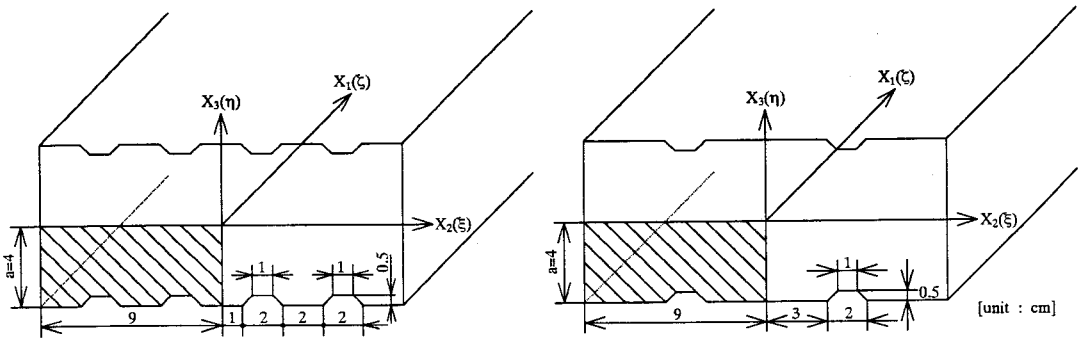

Case (A) Case(B)

Fig.1: Subject of calculation and coordinate system

of cellular secondary motion clear.

2.TECHNIQUE OF ANALYSIS

2.1 Subject of Numerical Analysis

As the subject of this numerical study, we have chosen the available experimental data for the fully developed turbulent flow in a rectangular duct with sand ridges presented by Nezu and Nakagawa [7]. Figure 1 shows the orthogonal coordinate system set in the rectangular duct and a schematic diagram of the experimental apparatus. Two kinds of flows with sand ridges were prepared as Case(A) and Case(B), in which the ridge spacing l was set equal to $l = a$ and $l = 2a$ (a is defined as half vertical width of conduit), respectively. The experimental duct has a 8 cm × 18 cm rectangular cross section and is 6 m in length. The test section was set up 4.8 m downstream from the entrance of the conduit. At this position the fully developed turbulent flow is approximately obtained by setting several tripping wires at the entrance. Reynolds number $Re = U_{1\max}a/\nu$, where $U_{1\max}$ is the maximum mainstream velocity and ν is the kinematic viscosity of air, is set to be 1.3×10^4. Measurements were conducted at 280 (Case(A)) and 340 (Case(B)) measuring points by hot wire anemometer.

In Fig.1, ξ, η, and ζ are the transformed coordinate axes of the boundary-fitted coordinate system, and X_1, X_2 and X_3 are the coordinates along the mainstream, in the spanwise and the vertical directions , respectively.

2.2 Reynolds Stress Model

The anisotropy nature of the turbulence is expressed by the Reynolds stress equations. Nevertheless, the exact solution of these equations is not yet available, and some modeling effort is required. A set of differential equations governing the transport of the Reynolds stresses is derived from the Navier-Stokes equation, namely:

$$\frac{\mathrm{D}\overline{u_iu_j}}{\mathrm{D}t} = -\left[\overline{u_iu_k}\frac{\partial U_j}{\partial X_k} + \overline{u_ju_k}\frac{\partial U_i}{\partial X_k}\right] + \overline{\frac{p}{\rho}\left\{\frac{\partial u_i}{\partial x_j} + \frac{\partial u_j}{\partial x_i}\right\}}$$
$$-\frac{\partial}{\partial x_k}\left[\overline{u_iu_ju_k} - \nu\frac{\partial\overline{u_iu_j}}{\partial x_k} - \overline{\frac{p}{\rho}(\delta_{jk}u_i + \delta_{ik}u_j)}\right] - 2\nu\overline{\frac{\partial u_i}{\partial x_k}\frac{\partial u_j}{\partial x_k}} \qquad (1)$$

The first term of the right hand side is the production term P_{ij}, the second is the pressure strain correlation π_{ij}, the third is the diffusion term, and the forth is the dissipation term ε_{ij}. It is difficult to obtain the solution of the Reynolds stress equation in the form presented above is difficult, and necessary to introduce model assumptions for the correlations appearing in the exact equations. For modeling of the convective and diffusion terms, the approximation by Rodi [14] was employed, by which these terms expressed in differential form of the Reynolds stress components are transformed into the algebraic equation. A particularly problematic task here is the modeling of the pressure–strain correlation term which includes the redistribution term. Following Chou [15], this term is expressed as follows:

$$\overline{\frac{p}{\rho}\frac{\partial u_i}{\partial u_j}} = \frac{1}{4\pi}\int_{\mathrm{vol}}\left[\overline{\left(\frac{\partial^2 u_\ell u_m}{\partial x_\ell \partial x_m}\right)'\frac{\partial u_i}{\partial x_j}} + 2\left(\frac{\partial U_\ell}{\partial x_m}\right)'\overline{\left(\frac{\partial u_m}{\partial x_\ell}\right)'\left(\frac{\partial u_i}{\partial x_j}\right)}\right]\frac{\mathrm{d\,vol}}{|\boldsymbol{x}-\boldsymbol{y}|} + S_{ij} \tag{2}$$

where the terms with and without the prime are related to the values at $\boldsymbol{y}$ and $\boldsymbol{x}$, respectively, and vol represents the volume of the subjected space. The first and second terms of the right hand side of (2) relate to the interactions of the fluctuating velocities and of the mean strain with the fluctuating velocities, respectively. The term S_{ij} represents the wall effect. In the present model, we adopted the Rotta's linear return-to-isotropy model for the first term of (2). His proposal for $\pi_{ij,1}$ is written as:

$$(\pi_{ij,1} + \pi_{ji,1}) = -c_1\frac{\varepsilon}{k}\left(\overline{u_i u_j} - \frac{2}{3}\delta_{ji}k\right) \tag{3}$$

where k and ε are the time-averaged turbulence kinetic energy and the energy dissipation rate, respectively, and c_1 represents an empirical constant.

For $\pi_{ij,2}$ the correlation is approximated in the form:

$$\pi_{ij,2} = \left(\frac{\partial U_\ell}{\partial x_m}\right)a_{\ell j}^{mi} \tag{4}$$

and $a_{\ell j}^{mi}$ is the forth-order tensor, which is determined by the following kinematic constraints:

$$a_{\ell j}^{mi} = a_{\ell j}^{im} = a_{j\ell}^{im} \tag{5}$$

$$a_{\ell i}^{mi}\frac{\partial U_\ell}{\partial x_m} = 0 \tag{6}$$

$$a_{jj}^{mi} = 2\overline{u_m u_i} \tag{7}$$

These constraints are different from the original Rotta's proposal in refer to the form of (6). We adopted them for the reason that $\pi_{ij,2}$ is defined as the product between the forth order tensor and the mean strain as seen in (4). The constraints in the form of (5), (6) and (7) arise from the symmetricity condition, the mass conservation law and the Green's theorem, respectively. The form of (7) suggests that the forth-order tensor is approximated by linear combination of the Reynolds stresses. The most general such tensor satisfying the symmetricity constraints implied by (7) is written as:

$$\begin{aligned} a_{\ell j}^{mi} = {} & \alpha\delta_{\ell j}\overline{u_m u_i} + \beta\left(\delta_{m\ell}\overline{u_i u_j} + \delta_{mj}\overline{u_i u_\ell} + \delta_{i\ell}\overline{u_m u_j} + \delta_{ij}\overline{u_m u_\ell}\right) \\ & + c_2\delta_{mi}\overline{u_\ell u_j} + \left\{\eta\delta_{mi}\delta_{\ell j} + v(\delta_{m\ell}\delta_{ij} + \delta_{mj}\delta_{i\ell})\right\}k \end{aligned} \tag{8}$$

which was derived by Launder, Reece, and Rodi [16], where δ_{ij} represents Kronecker delta and c_2, α, β, η, v are empirical constants. The application of (6) and (7) enables two constants of (8) to be expressed in terms of c_2. On combining (4) and (8), the complete influence of the mean strain on the pressure-strain correlation may be expressed in the following form:

$$(\pi_{ij,2} + \pi_{ji,2}) = -(\alpha+\beta)\left(P_{ij} - \frac{2}{3}P_k\delta_{ij}\right) + \zeta\left(\frac{\partial U_i}{\partial x_j} + \frac{\partial U_j}{\partial x_i}\right)k$$
$$+(4\beta+\alpha)\left(D_{ij} - \frac{2}{3}P_k\delta_{ij}\right) \tag{9}$$

$$D_{ij} = -\overline{u_i u_k}\frac{\partial U_k}{\partial x_j} - \overline{u_j u_k}\frac{\partial U_k}{\partial x_i}, \qquad P_k = -\overline{u_k u_\ell}\frac{\partial U_k}{\partial x_\ell}$$

$$\alpha = \frac{1}{11}(4c_2 + 10), \quad \beta = -\frac{1}{11}(2 + 3c_2), \quad \zeta = \eta + v.$$

In the above equation, ζ is an independent constant to be determined from experimental data and α and β are defined as functions of c_2. Contrary to this, in Launder, Reece and Rodi model, ζ, α and β are defined as a function of only c_2. Therefore, in the present model, we can take into account more experimental data than theirs.

The wall effect term $\pi_{ij,w}$ on turbulent stresses is determined in this model using the empirical constants as a function of the dimensionless distance from the wall:

$$\begin{aligned} c_1 &= c_1^* + c_1' f(L/x_w) \\ c_2 &= c_2^* + c_2' f(L/x_w) \\ \zeta &= \zeta^* + \zeta' f(L/x_w) \end{aligned} \tag{10}$$

$$f\left(\frac{L}{x_w}\right) = \frac{c_\mu^{3/4} k^{3/2}}{\kappa\varepsilon}\frac{1}{x_w} \tag{11}$$

where $f(L/x_w)$ is a function of the dimensionless wall distance and c_μ, κ represent the empirical constant and the von Karman constant, respectively. It expresses the influence of the wall and takes the value 1 in its vicinity, and approaches to 0 with increase of the distance. The symbol x_w expresses the distance from the wall and L defines the length scale of turbulence. The values of these constants are chosen such that, when $f = 0$, the model yields the correct Reynolds stress components for nearly homogeneous shear flow of Champangne, Harris and Corrsin [17], and, when $f = 1$, the relative magnitude of the stress components agrees with consensus of near wall turbulence. Moreover, we have used the experimental data of Harris, Graham and Corrsin [18] who reported further homogeneous shear flow data where the strain rate was higher than Champagne, Harris and Corrsin. The pressure-strain correlation terms and constants used in this analysis are summarized in the Tables 1 and 2, respectively.

The forth term of (1) is the homogeneous part of dissipation. This term is modeled commonly with the assumption of the isotropic motion for the dissipation, namely:

$$\varepsilon_{ij} = 2\nu\overline{\frac{\partial u_i}{\partial x_k}\frac{\partial u_j}{\partial x_k}} = \frac{2}{3}\delta_{ij}\varepsilon \tag{12}$$

Table 1: Modeling of the pressure-strain correlation terms

$\pi_{ij,1} + \pi_{ji+1}$	$-c_1 \frac{\varepsilon}{k}\left(\overline{u_i u_j} - \frac{2}{3}k\delta_{ji}\right)$
$\pi_{ij,2} + \pi_{ji,2}$	$-\frac{c_2+8}{11}\left(P_{ij} - \frac{2}{3}P_k\delta_{ij}\right) + \zeta k\left(\frac{\partial U_i}{\partial x_j} + \frac{\partial U_j}{\partial x_i}\right)$ $-\frac{8c_2-2}{11}\left(D_{ij} - \frac{2}{3}P_k\delta_{ij}\right)$
$[\pi_{ij} + \pi_{ji}]_w$	$c_1 = c_1^* + c_1' f\left(\frac{L}{x_w}\right),\quad c_2 = c_2^* + c_2' f\left(\frac{L}{x_w}\right),\quad \zeta = \zeta^* + \zeta' f\left(\frac{L}{x_w}\right)$

Table 2: Constants in the pressure-strain correlation terms

c_1^*	C_2^*	ζ^*	c_1'	c_2'	ζ'
1.4	0.44	-0.16	-0.35	0.12	-0.1

2.3 Boundary-Fitted Coordinate System

In order to calculate flows around complex figures, it is very difficult to set precisely the boundary condition along complex configuration, and boundary-fitted coordinate system (BFC) is adopted in this research. BFC technique consists of coordinate transformation from the analysis domain on the physical level to the calculation domain, and solving the governing equations on the calculation level. Although the setting of the boundary conditions and the discretization of the equations are easy in BFC, the transformed governing equations are characteristically complicated. It is better to construct the coordinates vertically each other in order to achieve good numerical stability and convergence. From this point of view, grid generation method based on the Poisson equation was adopted [19].

The governing equations are transformed to the calculation level according to the following mathematical definitions:

$$\frac{\partial}{\partial x_i} = \frac{\partial \xi}{\partial x_i}\frac{\partial}{\partial \xi} + \frac{\partial \eta}{\partial x_i}\frac{\partial}{\partial \eta} + \frac{\partial \zeta}{\partial x_i}\frac{\partial}{\partial \zeta} \tag{13}$$

For example, the momentum equation in the form including the Reynolds stress is transformed as follows:

$$\frac{\mathrm{D}U_i}{\mathrm{D}t} = -\frac{1}{\rho}\frac{\partial P}{\partial x_i} + \frac{\partial}{\partial x_j}\left(\nu\frac{\partial U_i}{\partial x_j} - \overline{u_i u_j}\right) \tag{14}$$

The Reynolds stress term in (14) is divided into two terms containing the velocity gradient and the remaining term.

$$-\overline{u_i u_j} = \left(\frac{b}{a}\right)_{ij}\frac{\partial U_i}{\partial x_j} - \left(\frac{c}{a}\right)_{ij} \tag{15}$$

In the above equation, a and b denotes the coefficients of the Reynolds stresses and the velocity gradient, respectively, and c represents the remaining term except these terms, as seen in (15). Here, including the Reynolds stress as part of the diffusion term and in order to attain stability

of the solution, we put:

$$d_{ij} = \nu + \left(\frac{b}{a}\right)_{ij} \qquad e_{ij} = \left(\frac{c}{a}\right)_{ij} \tag{16}$$

so that the momentum equation can be rewritten in the following form:

$$\frac{\partial U_i}{\partial t} + \frac{\partial U_i U_j}{\partial x_j} = -\frac{1}{\rho}\frac{\partial P}{\partial x_i} + \frac{\partial}{\partial x_j}\left\{d_{ij}\frac{\partial U_i}{\partial x_j} - e_{ij}\right\} \tag{17}$$

Applying this formula to the mathematical definition of (13) shown above, it is finally transformed to:

$$\begin{aligned}
&\frac{\partial U_i}{\partial t} + \frac{\partial}{\partial \xi}\left\{\boldsymbol{U}U_i + \frac{P}{\rho}\xi_{xi} - l_1 U_{i\xi} - l_2 U_{i\eta} - l_3 U_{i\zeta} + \xi_x e_{i3} + \xi_y e_{i2} + \xi_z e_{i1}\right\} \\
&\quad + \frac{\partial}{\partial \eta}\left\{\boldsymbol{V}U_i + \frac{P}{\rho}\xi_{xi} - l_2 U_{i\xi} - l_4 U_{i\eta} - l_5 U_{i\zeta} + \eta_x e_{i2} + \eta_y e_{i2} + \eta_z e_{i1}\right\} \\
&\quad + \frac{\partial}{\partial \zeta}\left\{\boldsymbol{W}U_i + \frac{P}{\rho}\xi_{xi} - l_3 U_{i\xi} - l_5 U_{i\eta} - l_6 U_{i\eta} + \zeta_x e_{i\zeta} + \zeta_y e_{i2} + \zeta_2 e_{i1}\right\} = 0
\end{aligned} \tag{18}$$

$$\begin{aligned}
l_1 &= d_{i3}\xi_{x3}^2 + d_{i2}\xi_{x2}^2 + d_{i1}\xi_{x1}^2 \\
l_2 &= d_{i3}\xi_{x3}\eta_{x3} + d_{i2}\xi_{x2}\eta_{x2} + d_{i1}\xi_{x1}\eta_{x1} \\
l_3 &= d_{i3}\xi_{x3}\zeta_{x3} + d_{i2}\xi_{x2}\zeta_{x2} + d_{i1}\xi_{x1}\zeta_{x1} \\
l_4 &= d_{i3}\eta_{x3}^2 + d_{i2}\eta_{x2}^2 + d_{i1}\eta_{x1}^2 \\
l_5 &= d_{i3}\eta_{x3}\zeta_{x3} + d_{i2}\eta_{x2}\zeta_{x2} + d_{i1}\eta_{x1}\zeta_{x1} \\
l_6 &= d_{i3}\zeta_{x3}^2 + d_{i2}\zeta_{x2}^2 + d_{i1}\zeta_{x1}^2
\end{aligned} \tag{19}$$

$$\begin{aligned}
\boldsymbol{U} &= U_1\frac{\partial \xi}{\partial x_1} + U_2\frac{\partial \xi}{\partial x_2} + U_3\frac{\partial \xi}{\partial x_3} \\
\boldsymbol{V} &= U_1\frac{\partial \eta}{\partial x_1} + U_2\frac{\partial \eta}{\partial x_2} + U_3\frac{\partial \eta}{\partial x_3} \\
\boldsymbol{W} &= U_1\frac{\partial \zeta}{\partial x_1} + U_2\frac{\partial \zeta}{\partial x_2} + U_3\frac{\partial \zeta}{\partial x_3}
\end{aligned} \tag{20}$$

where $\boldsymbol{U}$, $\boldsymbol{V}$ and $\boldsymbol{W}$ are components of the contravariant velocity. The symbol l represents the metric tensor appearing as a result of transformation. In the case of three dimensional flows, nine diffusion coefficients are needed. For the other governing equations, application of the same steps leads to the transformed equations on the calculation level.

2.4 Method of Numerical Analysis

Numerical analysis has been carried out for Reynolds number $Re = 1.3\times10^4$, which is same as the experiment referred, which treated the developing turbulent flow in a rectangular duct of aspect ratio 2.25:1. The length of the entrance section was of 100 D_h (D_h represents the hydraulic diameter). Considering the symmetry of the rectangular duct, the region of calculation, shaded zone in Fig.1, corresponds to 1/4 of the whole cross section. Figure 2 shows

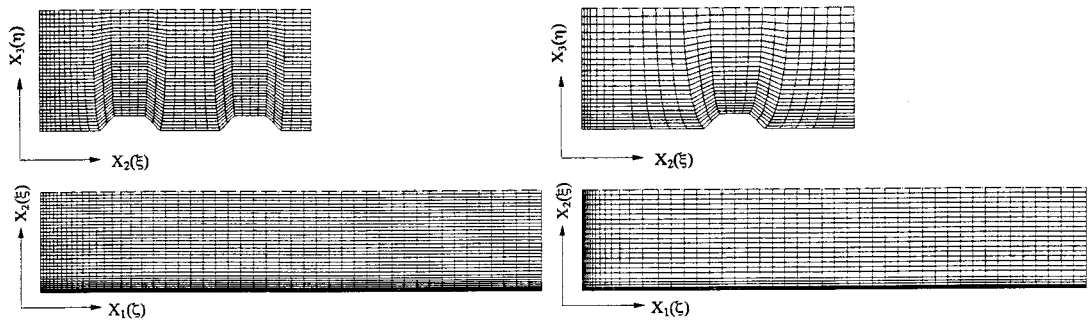

Case (A) Case (B)

Fig.2: Arrangement of calculation mesh

the grid mesh over the rectangular duct cross section with sand ridges. The mesh number of Case(A) and Case(B) are $\xi \times \eta \times \zeta = 35 \times 35 \times 50$, $25 \times 25 \times 50$, respectively. Since the both results of 25×25 mesh and 35×35 mesh over the quadrant of same rectangular duct coincide with the experimental data without large discrepancy as described in later, the grid dependency is not examined in detail. It may be said that the characteristic feature of this kind of flows is able to be predicted by setting such grid number as used in this research.

An isotropic turbulent flow with constant velocities is assumed at the inlet. Since the turbulent energy k and the turbulent dissipation ε are unknown from the experimental data, values of $k = U_b \times 10^{-5}$, $\varepsilon = k^{3/2}/D_h$ were adopted at the inlet section (U_b denotes the bulk velocity). The Neumann conditions were used at the outlet section. As for the boundary conditions for k and ε equations, the consistency of the universal velocity distribution at the vicinity of the wall and also the supposition of the local equilibrium lead to utilization of the law of wall function.

The governing equations are discretized by finite difference method. The QUICK (quadratic interpolation for convective kinematics) approximation of Leonard [20] is used for discretizing the convective transport term and the other terms are discretized by central-difference scheme. In numerical solution, implicit method is adopted and SOR (successive over relaxation) method is utilized as a solution of the algebraic equations.

3. ANALYSIS RESULTS AND CONSIDERATIONS

3.1 Comparison of Time Averaged Velocity

Calculated results of the contour map of mean velocity and the experimental results of Nezu-Nakagawa [7] are shown in Fig.3. These results were nondimensionalized by the maximum mean flow velocity $U_{1\max}$ at each cross section. These contour maps are of the turbulent flows with two sand ridges Case(A) and with single ridge Case(B) in a quarter cross section. In numerical analysis, flow developments are presented at the locations $X_1 = 6.2\,D_h$, $22.5\,D_h$ and $95.0\,D_h$ from the entrance. The experimental data [7] were measured at fully developed turbulent region.

At the location $X_1 = 6.2\,D_h$, the contour lines over the ridge are distorted like a cavity

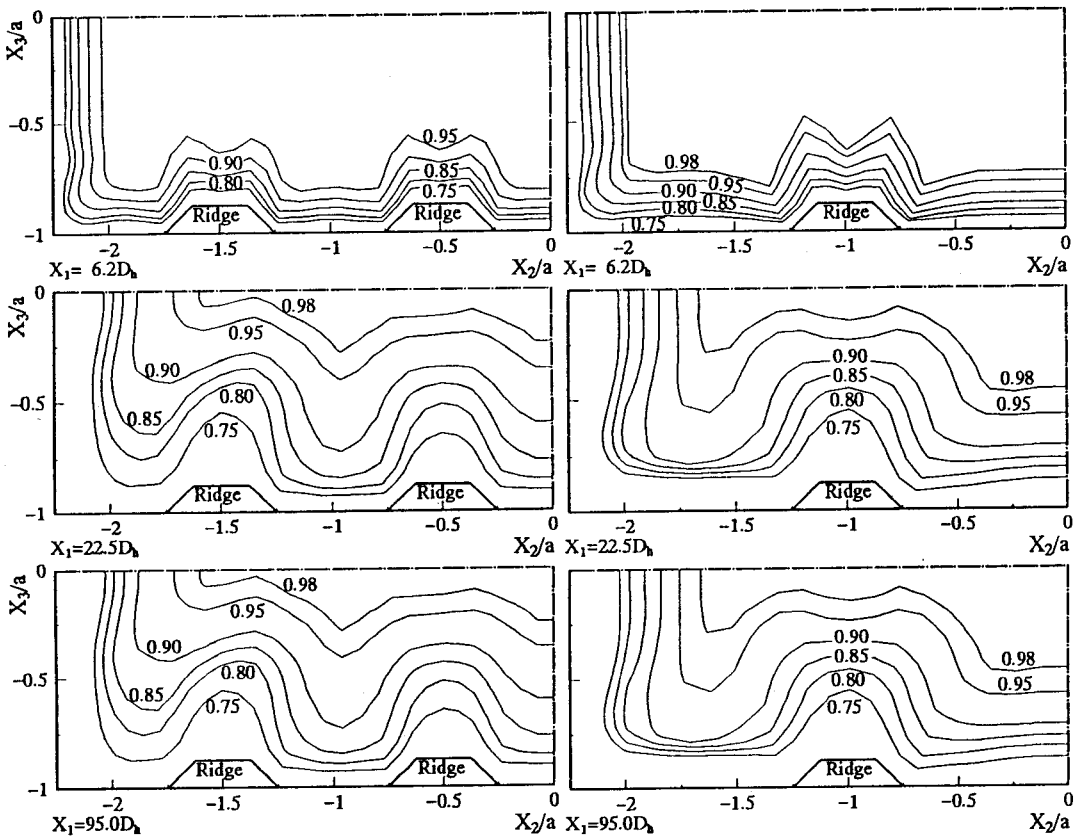

Numerical results of X_1/D_h = 6.2, 22.5 and 95.0

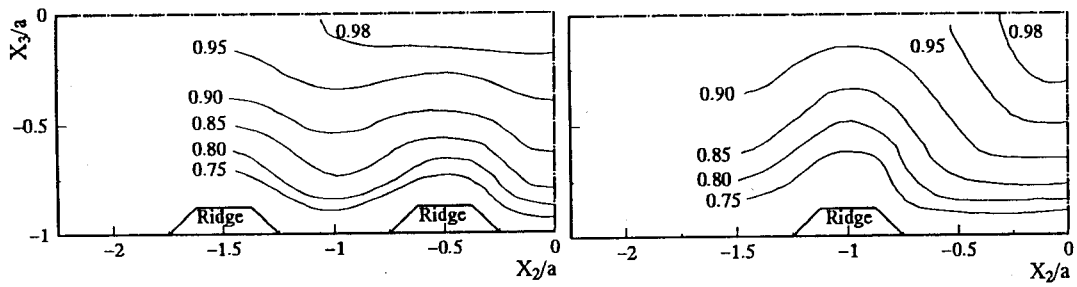

Experiment by Nezu and Nakagawa [7]

(a) Case(A) (b) Case(B)

Fig.3: Mean flow velocity

in both cases(A) and (B). At the $X_1 = 22.5\,D_h$ further downstream the contour lines develop toward the upper bisector from the bottom wall of conduit. At this location, distorted lines over the ridges are not observable anymore. Numerical results indicate periodic variation in spanwise direction. The contour lines at $X_1 = 95.0\,D_h$, which corresponds to the fully developed

region, show the similar feature at the location $X_1 = 22.5\,D_h$. The vertical derivatives of the mean velocity over ridges is small, and those over troughs shows large value. In other words, the low-speed region is formed on longitudinal ridge, while the high-speed region is on longitudinal trough. Comparing these numerical results of fully developed turbulent flow with the experimental data, it is said that the agreements are reasonably good except for iso-lines near the central region of the conduit with single ridge.

Figure 4 shows the secondary flow vectors for developing turbulent flow in Case(A) and Case(B) at the same location in Fig.3. As the flow develops, the secondary flow toward the corner region and ridges are formed in both cases. They indicate a cellular structure that has a pair of counter-rotating streamwise vortices.

As mentioned above, the distortion of the mean velocity over ridges are observed like a cavity at $X_1 = 6.2\,D_h$. From Fig.4 of the secondary vectors, this phenomenon may be caused by fact that the upward velocity over ridges is smaller than those at both sides of ridges. As the flow develops downstream further, the upward velocity over the ridge becomes larger, and this increasing of upward velocity push up the distorted iso-lines toward the upper bisector.

At the location $X_1 = 22.5\,D_h$ and $95.0\,D_h$, a pair of counter-rotating streamwise vortices is clearly recognized. Since the region of upflow over the ridge is narrower than that of downflow over the trough, the upflow is much stronger than the downflow. This remarkable feature of stronger upflows in a narrow zone and weaker downflows in the surrounding wide zone is recognized in both of the numerical and experimental results, and this has been also observed in real rivers. This phenomenon is interpreted as one of the special features in a rectangular duct with sand ridges.

Moreover, the secondary flow near the left-hand side ridge in Case(A) has larger value than the one in Case(B) has. This may be interpreted that the secondary flow over the left-hand side ridge is accelerated by the secondary flow generated near the corner region. From numerical and experimental results, it is found that the intensity of the secondary flow near the ridges is larger than that of the corner region. This fact suggests that artificial ridges attached on heat exchanger ducts are useful for promoting heat and mass transfer without much pressure loss. Furthermore, the generation mechanism of sand ridges is proposed as follows: The first sand ridge is generated near the corner due to the secondary currents of the corner region. Then, a pair of secondary flow is generated over the first sand ridge due to anisotropic turbulence. Nextly, this secondary flow over the first sand ridge induces the flow toward the wall bisector along the river bed, and thus induced flow forms the second sand ridge near the first one. The third and fourth sand ridges are produced successively following the same mechanism.

Experimental data clearly show that the center of vortices in Case(A) exists at lower position than that of Case(B). The present numerical analysis also estimates the locations of vortices without large discrepancy.

Recently, the turbulent flow of blade riblet with rectangular cross section has been calculated by Launder and Li [21]. Their calculated results show that the secondary currents proceed downward from the upper wall to the top of the blade riblet with counter-cloclwise vortex on the right side of blade. Their calculated results agree with the experimental data measured by Nakamura *et al.* [22], who have measured the turbulent flow of blade riblet with cross section. These results suggest that the secondary flow of the second kind is sensitively influenced by

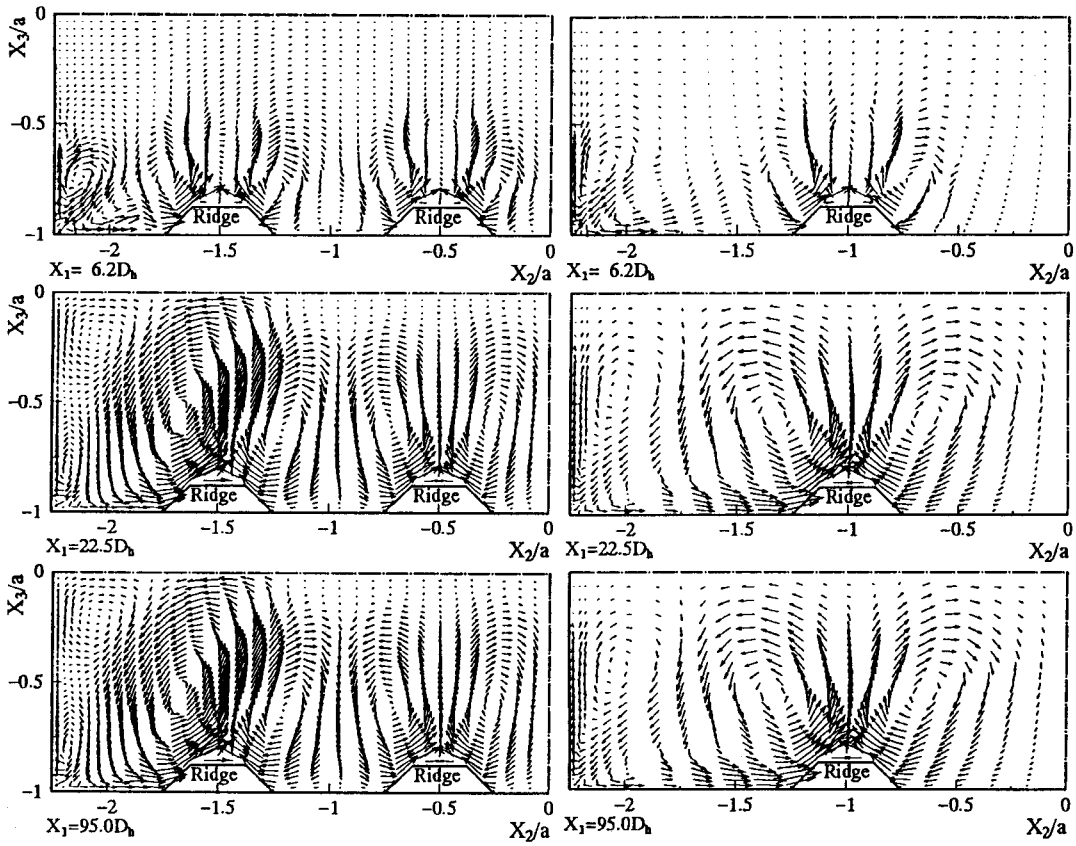

Numerical results of $X_1/D_h = 6.2$, 22.5 and 95.0

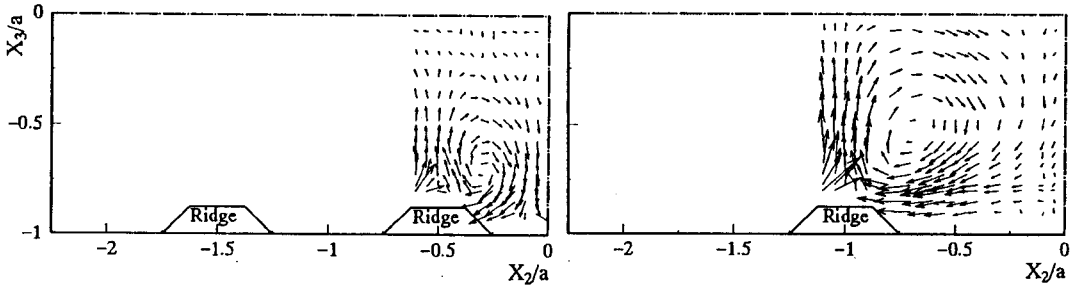

Experiment by Nezu and Nakagawa [7]

Case(A) Case(B)

Fig.4: Secondary flow vectors

geometry of the cross section.

Figure 5 shows the spanwise distribution of the friction velocity U_*, which is evaluated from

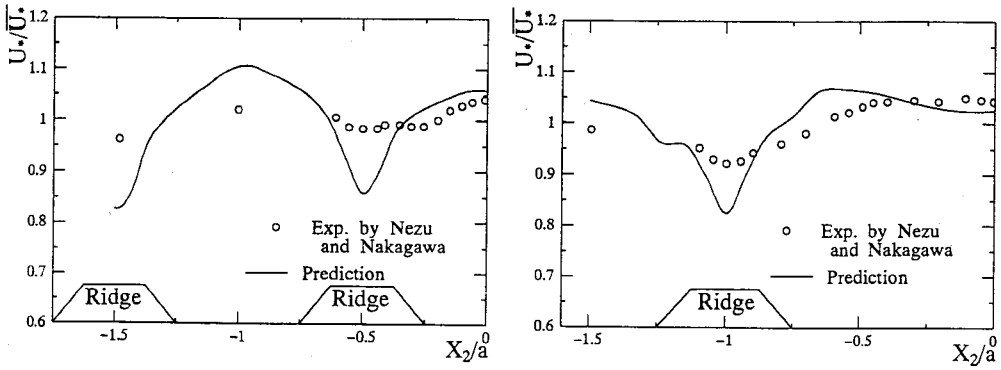

(a) Case (A) (b) Case (B)

Fig.5: Distribution of friction velocity

the following relation:

$$\frac{U_1}{U_*} = 5.75 \log \left(\frac{U_* y}{\nu} \right) + 5.5 \tag{21}$$

where y is defined as the vertical coordinate from the local bed. In Fig.5, the numerical as well as experimental results of Case(A) and Case(B) are presented. The friction velocity and bed shear stress are larger in the troughs where the downflows exist, and smaller over the ridges where the upflows occur. This increase of friction velocity in regions with downflow is due to downflow transport of high momentum fluid toward the bed and hence the local velocity gradients are higher. These facts suggest that sands on the troughs are swept out from each side of the troughs due to high wall shear stress. In turn, fine sands on the ridges may be intermittently lifted up to the free surface by the strong upflow. This phenomenon may be "boils" with high sediment concentrations. If periodically spaced longitudinal ridges and troughs are present in wide straight channel, the bed shear stress may vary periodically in the spanwise direction. In comparison with the experimental results, the numerical results show a tendency to predict the smaller friction velocity over the ridges.

3.2 Comparison of Reynolds Stress

For steady, incompressible, fully developed turbulent flow of constant-property fluid, the vorticity transport equation for streamwise vorticity is expressed as follows:

$$U_2 \frac{\partial \omega_1}{\partial x_2} + U_3 \frac{\partial \omega_1}{\partial x_3} = \frac{\partial^2}{\partial x_2 \partial x_3} \left(\overline{u_2^2} - \overline{u_3^2} \right) + \left(\frac{\partial^2}{\partial x_3^2} - \frac{\partial^2}{\partial x_2^2} \right) \overline{u_2 u_3} + \nu \left(\frac{\partial^2 \omega_1}{\partial x_2^2} + \frac{\partial^2 \omega_1}{\partial x_3^2} \right) \tag{22}$$

where the components of the vorticity vector are:

$$\omega_1 = \frac{\partial U_3}{\partial x_2} - \frac{\partial U_2}{\partial x_3}, \quad \omega_2 = \frac{\partial U_1}{\partial x_3} - \frac{\partial U_3}{\partial x_1}, \quad \omega_3 = \frac{\partial U_2}{\partial x_1} - \frac{\partial U_1}{\partial x_2} \tag{23}$$

In the above equation of fully developed flow, it is seen that the secondary flow of the second kind is caused by anisotropy of the turbulent stresses, namely, by the contributions of the first and second terms of the right hand side of (22).

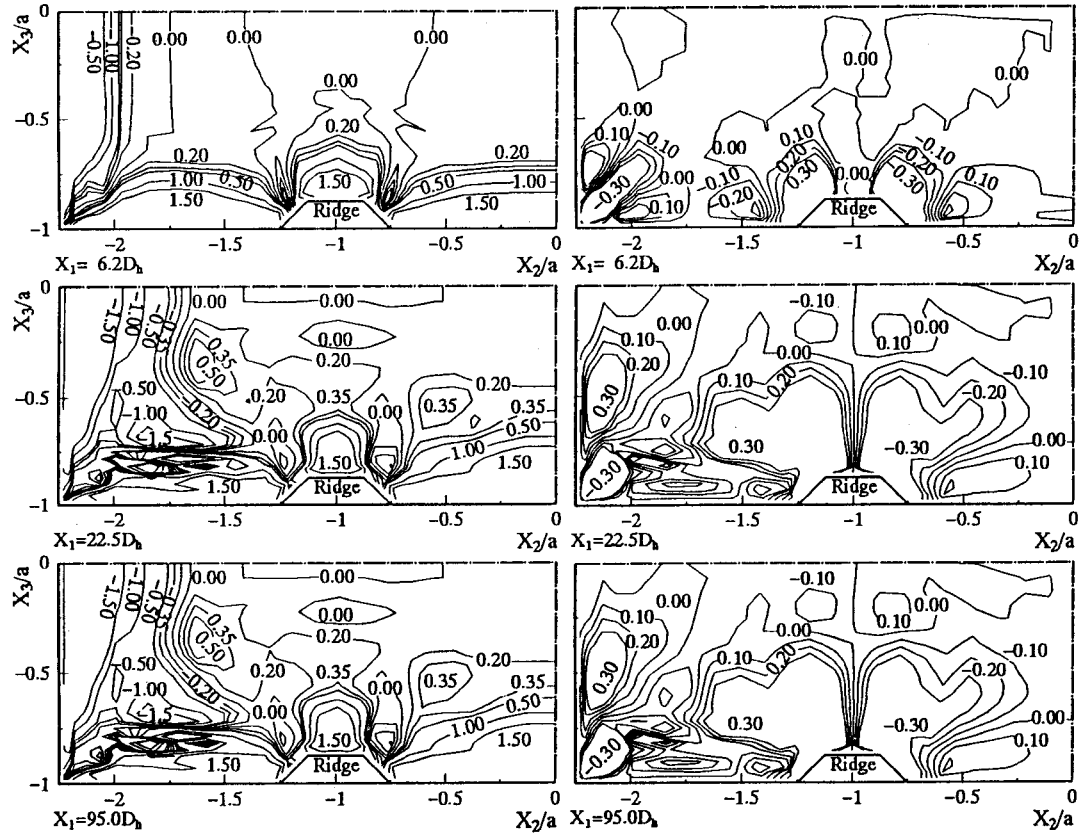

Numerical results of X_1/D_h = 6.2, 22.5 and 95.0

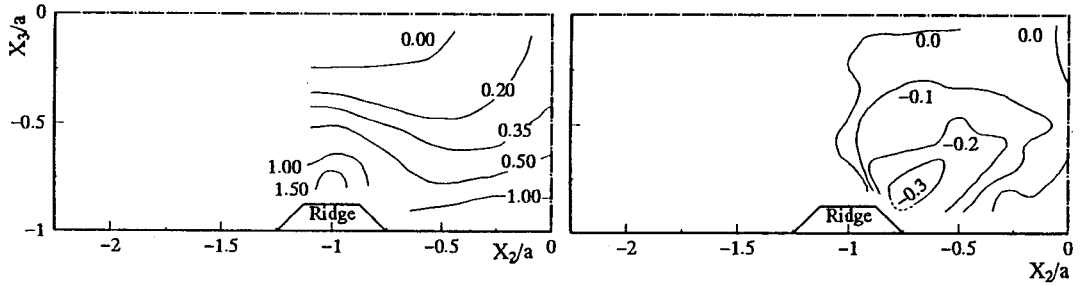

Experiment by Nezu and Nakagawa [7]

(a) $\left(\overline{u_2^2} - \overline{u_3^2}\right)$ (b) $\overline{u_2 u_3}$

Fig.6: Contour lines of $\left(\overline{u_2^2} - \overline{u_3^2}\right)$ and $\overline{u_2 u_3}$ for Case(B)

Figure 6 shows the contour lines of the difference between $\overline{u_2^2}$ and $\overline{u_3^2}$ (a) and the shear stress $\overline{u_2 u_3}$ (b) in Case(B) for developing and fully developed turbulent flow, and the experimental results are also shown for fully developed turbulent region. In the experiment, $(\overline{u_2^2} - \overline{u_3^2})$ reaches a maximum near the bed of the ridge, and becomes smaller and flatter over the troughs. On the other hand, numerical results show that the high absolute value exists not only over ridge but also over troughs and side wall. In both results, in the region near the upper wall bisector, $\overline{u_3^2} > \overline{u_2^2}$ over the ridge, while $\overline{u_2^2} > \overline{u_3^2}$ over the troughs. This suggests that $\overline{u_3^2}$ increases over the ridges due to the upflow extending up to near the upper wall bisector. Large discrepancy between the experimental and calculated is interpreted that the negative values of $(\overline{u_2^2} - \overline{u_3^2})$ by the numerical results appear symmetrically in both sides of the ridge, but the experimental data do not show such negative value. These negative values may be generated as a result of transport of the small normal stress $\overline{u_2^2}$ by the secondary flow.

Nextly, attention is paid for the shear stress $\overline{u_2 u_3}$ related to the generation of secondary currents, as shown in Fig.6(b). The contours of these shear stress are remarkably different from those of the difference between the normal stresses. Their peaks locate at the boundary between the ridge and trough. In numerical results, the contours of the shear stress over the ridge extend, as the flow develops, to the upper wall bisector from the ridge without destroying the symmetrical pattern.

Figure 7(a) and (b) show the contours of the shear stress $\overline{u_1 u_3}$ and $\overline{u_1 u_2}$ for developing turbulent flow in Case(A), respectively. The counter lines of $\overline{u_1 u_3}$ over ridges are greatly distorted at $X_1 = 22.5\, D_h$ and $X_2 = 95.0\, D_h$. These bulgings of contour lines are induced by the strong upward flow over ridges. Furthermore, the shear stress $\overline{u_1 u_3}$ develops from the bottom wall to the upper wall bisector as the river flows downstream, which is observed in the region between $X_1 = 6.2\, D_h$ and $X_1 = 22.5\, D_h$.

In addition, the shear stress $\overline{u_1 u_2}$ is examined. As shown in Fig.7(b), the contour lines of it display symmetrical pattern over the ridges. The positive value of shear stress is located in the left hand side of ridges and the negative value is generated in the right hand side of them. The contours over the ridge located near side wall is deformed without keeping the symmetrical pattern. This phenomenon suggests that the intensity of secondary current flowed from corner to ridge is stronger than that of the other secondary flow. The maximum value of this shear stress is formed near the side wall and the ridge located near the side wall. On the contrary to the shear stress $\overline{u_1 u_3}$, the present shear stress develops from the side wall toward the central region of conduit.

Figure 8(a) shows the shear stress $\overline{u_1 u_3}$ of numerical results compared with the experimental data for fully developed turbulent flow in Case(A). The locations $X_2/a = -0.05$, -0.1 and -0.2 correspond to trough near central region of conduit and $X_2/a = -0.3$, -0.4 and -0.5 correspond to right hand side ridge. Calculated results show that the maximum value of the shear stress appears at $X_2/a = -0.2$ which corresponds to the trough region. This fact is also found in the contour lines of the shear stress as shown in Fig.7. On the contrary, in the experimental data, the maximum value of it is formed at the upper part of ridge. Considering that the shear stress is defined as the product of the eddy viscosity and the derivative of the mean flow velocity with respect to X_3, its maximum value most likely be formed in the region of troughs where the velocity gradient of the mean flow is far larger than in other region. Except this discrepancy

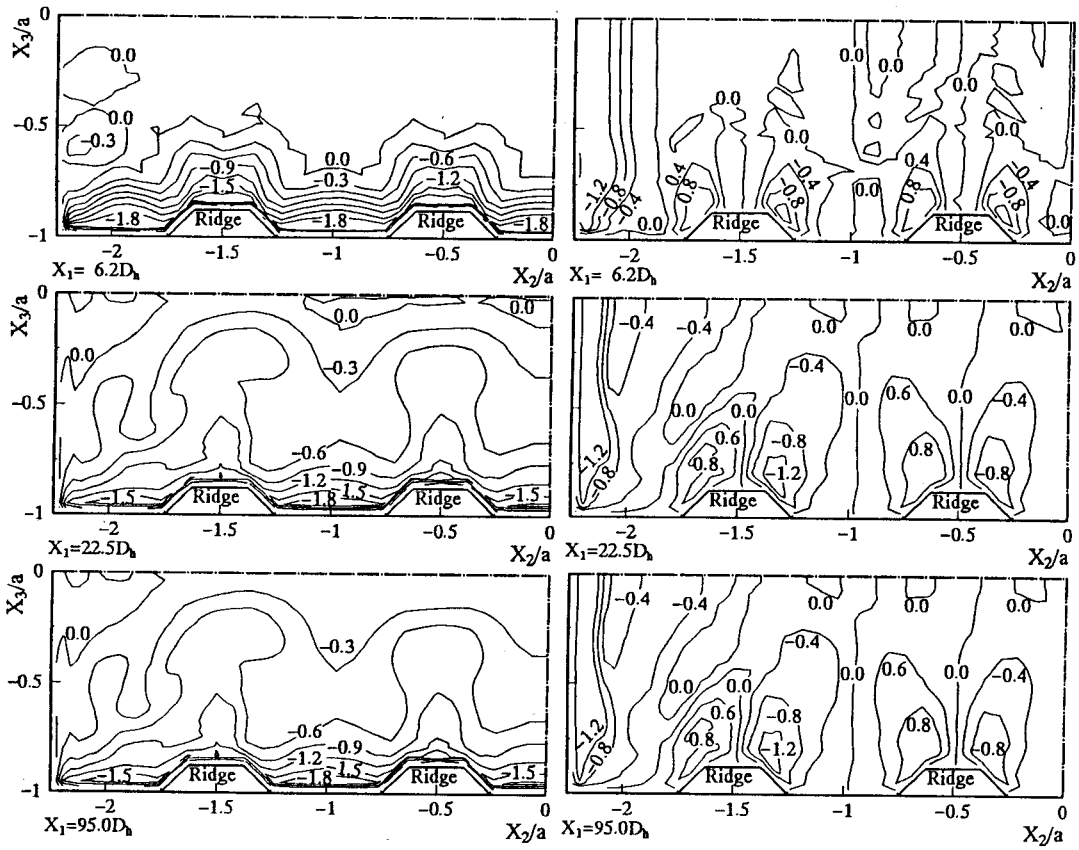

(a) $\overline{u_1u_3}$ (b) $\overline{u_1u_2}$

Fig.7: Contour lines of $\overline{u_1u_3}$ and $\overline{u_1u_2}$ for Case(A)

the present method predicts properly the experimental data.

Figure 8(b) shows the distribution of the shear stress $\overline{u_1u_2}$ of numerical results compared with the experimental data for fully developed turbulent flow in Case(A). The locations $X_2/a = -0.05$, -0.1 and -0.2 correspond to trough near the central region of conduit and $X_2/a = -0.3$, -0.4 and -0.5 correspond to right hand side ridge. With regard to the shear stress $\overline{u_1u_2}$, the present method underpredicts the experimental data.

Figure 9 shows the contours of the shear stress $\overline{u_2u_3}$ and the difference between $\overline{u_2^2}$ and $\overline{u_3^2}$ for developing turbulent flow in Case(A). These contour lines of the shear stress display the symmetric pattern over the ridges and its maximum absolute value is observed not over the side wall where the maximum absolute value of shear stress $\overline{u_1u_2}$ is recognized, but over the ridges and the corner region along the corner bisector. Not only the maximum absolute value but also the value of this shear stress is smaller than the other Reynolds stresses. As the flow develops, the large variation of this shear stress is not recognized, which is different from the other Reynolds stresses.

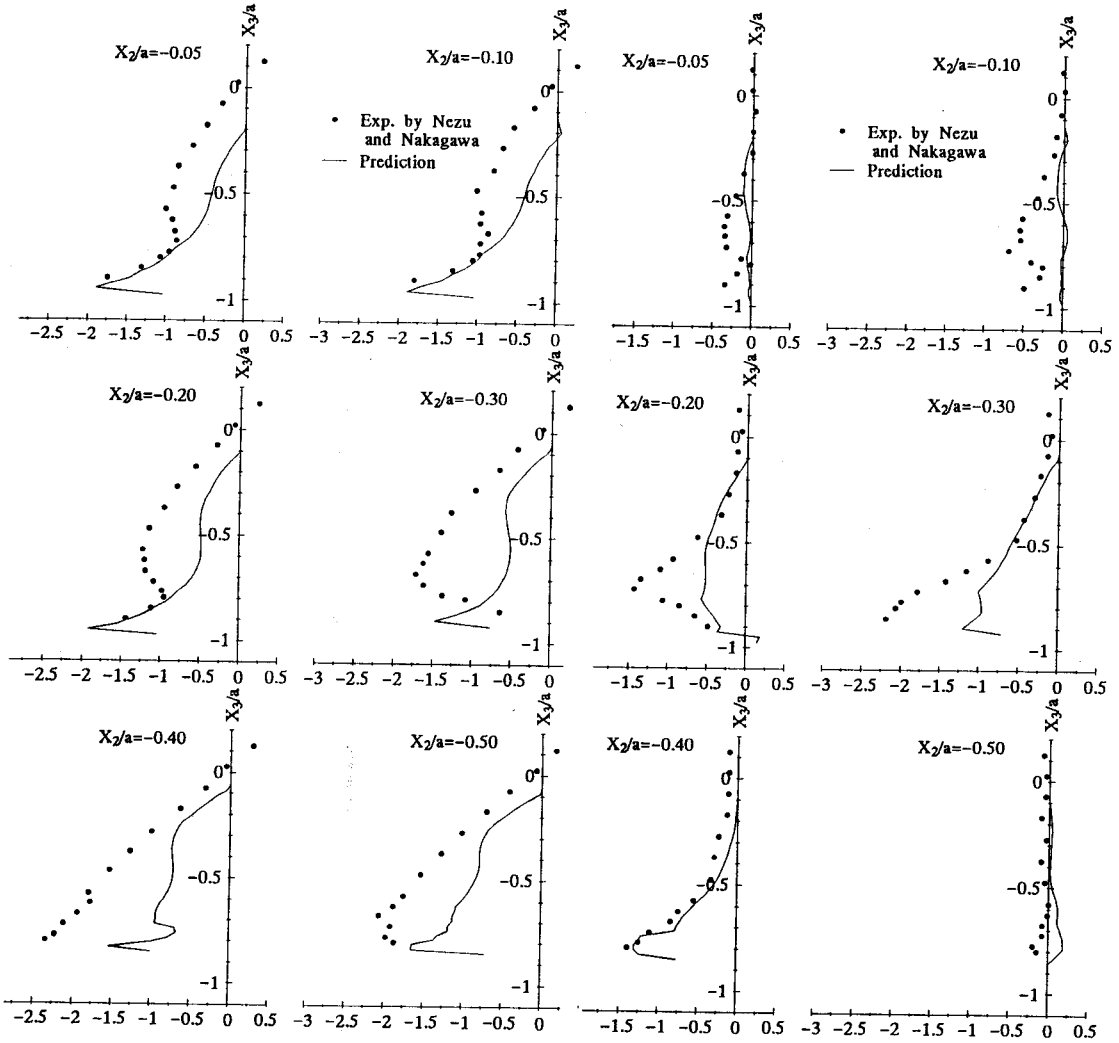

(a) $\overline{u_1 u_3}$ (b) $\overline{u_1 u_2}$

Fig.8: Distribution of $\overline{u_1 u_3}$ and $\overline{u_1 u_2}$ in Case (A)

As is already mentioned the above, the difference between $\overline{u_2^2}$ and $\overline{u_3^2}$ plays an important role in the generation of secondary currents as well as the shear stress $\overline{u_2 u_3}$. In this rectangular duct with two ridges, the maximum absolute value of $\left(\overline{u_2^2} - \overline{u_3^2}\right)$ is clearly located over the ridges, troughs and side walls as well as the rectangular duct with single ridge as shown in Fig.6. But, limiting to over troughs, the region of the maximum absolute value for the rectangular duct with single ridge is greater than that of the rectangular duct with two ridges. This discrepancy between Case(A) and Case(B) may be derived from the reason that the horizontal velocity fluctuations over trough are suppressed by two ridges located in both sides of trough

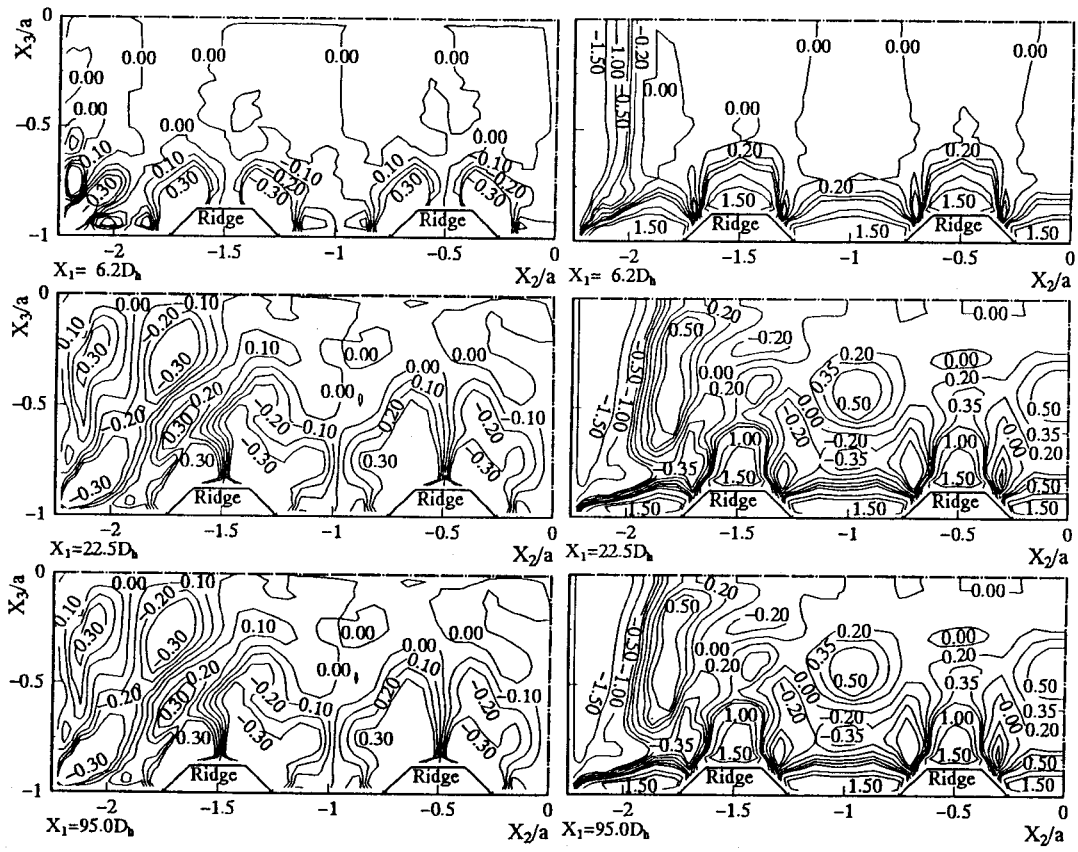

(a) $\overline{u_2u_3}$ (b) $\left(\overline{u_2^2} - \overline{u_3^2}\right)$

Fig.9: Contour lines of $\overline{u_2u_3}$ and $\left(\overline{u_2^2} - \overline{u_3^2}\right)$ for Case(A)

in Case(A). As a result of this suppression, the region of the maximum absolute $(\overline{u_2^2} - \overline{u_3^3})$ over trough becomes smaller than that of rectangular duct with single ridges.

Figure 10(a) compares the shear stress $\overline{u_2u_3}$ of numerical results with the experimental data for fully developed turbulent flow along the perpendicular axis to the bottom wall. Since the values of this shear stress are at least an order of magnitude smaller than other Reynolds stresses, it is very difficult to measure this shear stress, and the experimental data vary widely, especially for $X_2/a = -0.1$ and -0.5.

Figure 10(b) shows the numerical results of $(\overline{u_2^2} - \overline{u_3^2})$ and the experimental results for fully developed turbulent flow along the perpendicular axis to bottom wall in Case(A). At the location $X_1 = -0.3$ and -0.4 which corresponds to over the ridge of right hand side, the numerical results, which indicate negative value near the ridge, shows contrary tendency to the experimental data. This negative value is also recognized from numerical contour lines for fully developed turbulent flow as shown in Fig.9.

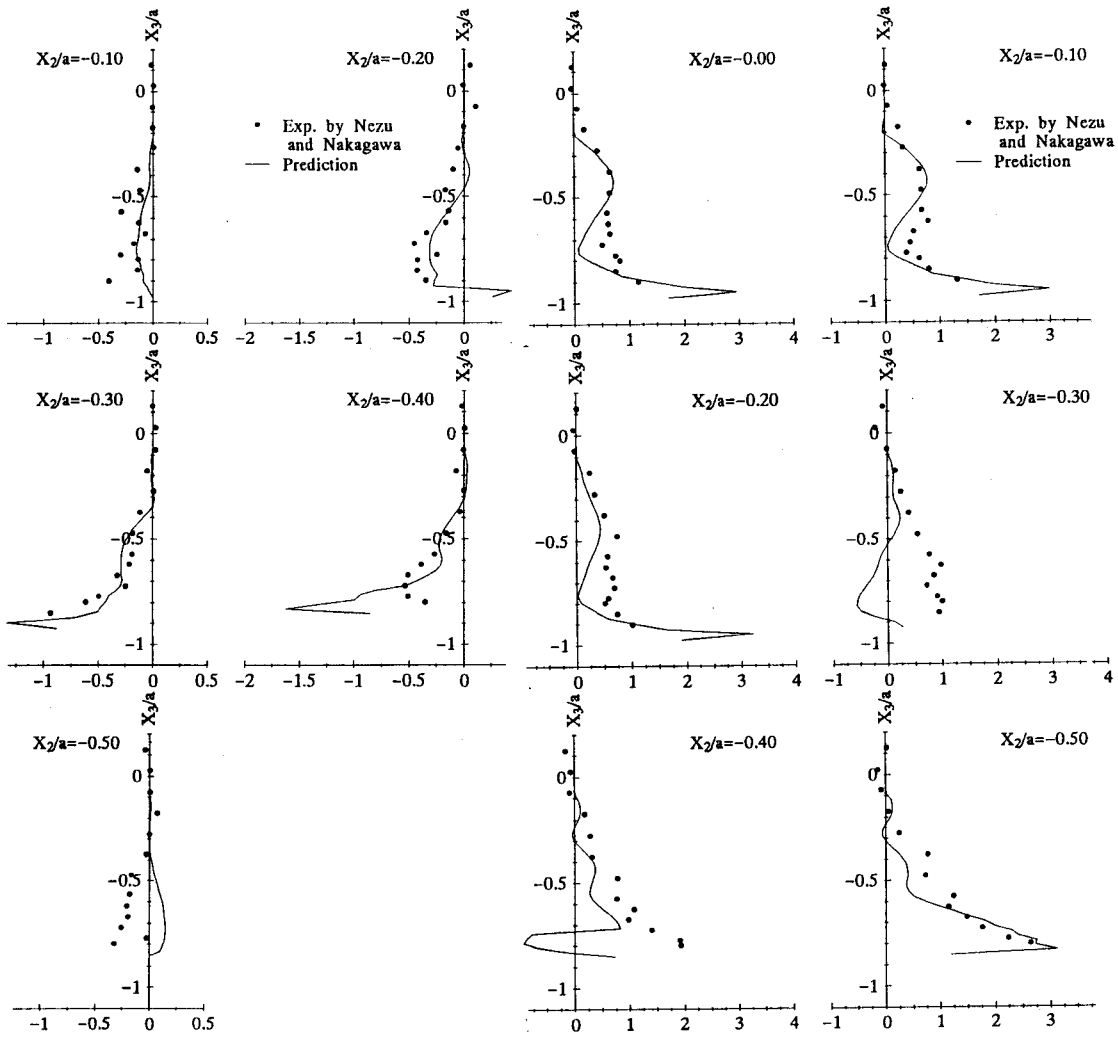

(a) $\overline{u_2u_3}$ (b) $\left(\overline{u_2^2} - \overline{u_3^2}\right)$

Fig.10: Distribution of $\overline{u_2u_3}$ and $\left(\overline{u_2^2} - \overline{u_3^2}\right)$ in Case(A)

4. CONCLUSIONS

The turbulence-driven secondary motion is considered as the characteristic feature of developing turbulent flow in non-circular ducts. Although this secondary velocity is only of order of two or three percent of the streamwise bulk velocity, its presence considerably displaces the lines of constant axial velocity toward the corners of the duct, and yields a relatively high velocity field there. This secondary motion proposes interesting phenomena in various engineering fields. In this research, special attention is paid for the developing turbulent flow in rectangular

duct with sand ridges, which has been extensively studied by river engineers. In calculation, boundary-fitted coordinate system is adopted in order to set the boundary condition properly and algebraic Reynolds stress model is introduced to predict anisotropic turbulence.

As a result of this calculation, it is concluded that the present method can predict the secondary currents over the ridges in two kinds of flow and the calculated results of the distribution of the Reynolds stresses are in good agreement with the experiment. The numerical results of secondary motions show that the intensity of the secondary flow over the ridges is larger than that of the corner region. This fact suggests that artificial ridges attached in the heat exchanger duct is useful for promoting heat and mass transfer without great pressure loss. Furthermore, considering the numerical and experimental results, the generation mechanism of sand ridges is discussed. The first sand ridge is generated near the corner region by the secondary currents of the corner region. Then a pair of secondary flow is induced over the first sand ridge by anisotropic turbulence. As the next step, this secondary flow over the first sand ridge induces the flow toward the wall bisector along the river bed, and second sand ridge is formed by this induced flow.

Acknowledgments

The authors wish to express their appreciation to Prof.I.Nezu and Prof.H.Nakagawa, Kyoto University, who kindly allowed us to use their experimental results in this paper and also provide us valuable suggestions and discussions on this numerical analysis.

REFERENCES

[1] V.A.Vanoni (1946) Transportation of suspended sediment by water; Trans., ASCE, vol.111 pp.67-133

[2] G.H.Matthes (1947) Macroturbulence in natural stream flow; Trans. Amer. Geophy. Union, vol.28 pp.255-265

[3] R.Kinoshita (1967) An analysis of the movement of flood waters by aerial photography,concerning characteristics of turbulence and surface flow; Photographic Surveying, vol.6 pp.1-17 (in Japanese)

[4] J.K.Culbertson (1967) Evidence of secondary circulation in an alluvial channel; US Geological Survey, Proc. Paper 575-D pp.D214-D216

[5] I.Karcz (1973) Reflections on the origin of source small-scale longitudinal streambed scours; Fluvial Geomorphology, vol.1973 pp.149-173

[6] A.Müller, X.Studerus (1979) Secondary flow in an open channel; Proc. 18th Conf. of IAHR, no.B.A.3, pp.19-24

[7] I.Nezu, H.Nakagawa (1984) Cellular secondary currents in straight conduit; J. Hydraulic Eng., ASCE, vol.110 pp.173-193

[8] D.Naot, W.Rodi (1982) Calculation of secondary currents in channel flow; J. hydraulic Eng.,ASCE, vol.108 no.HY8 pp.948-973

[9] A.O.Demuren, W.Rodi (1984) Calculation of turbulent-driven secondary motion in non-circular ducts; J. Fluid. Mech., vol.140 pp.189-222

[10] J.O.Hinze (1973) Experimental investigation of secondary currents in the turbulent flow through a straight conduit; Appl. Sci. Res., vol.28 pp.453-465

[11] H.Sugiyama, M.Akiyama, T.Serizawa (1991) Numerical analysis of developing flow in a

square duct using Reynolds stress model; Proc. ASME/JSME Thermal Eng. Joint Conf. 1991, vol.3 pp.159-165

[12] H.Sugiyama, M.Akiyama, N.Ninomiya, M.Hirta, k.Saitoh (1993) Numerical analysis of three dimensional flow in an elliptical duct by Reynolds stress model and boundary-fitted coordinate system; CFD Journal, vol.1 pp.429-442

[13] H.Sugiyama, M.Akiyama, M.Matsumoto, M.Hirata, N.Ninomiya (1993) Numerical analysis of fully developed turbulent flow in a square duct with two facing roughened walls; CFD Journal, vol.2 pp.319-338

[14] W.Rodi (1976) A new algebraic relation for calculating the Reynolds stresses; Z. Angew. Math. Mech., vol.56 pp.T219-T221

[15] P.Y.Chou (1945) On velocity correlations and the solutions of the equations of turbulent fluctuation; Quart. Appl. Math. vol.3 pp.38-54

[16] B.E.Launder, G.J.Reece, W.Rodi (1975) Progress in the development of a Reynolds stress turbulence closure; J. Fluid Mech., vol.68 pp.537-566

[17] F.H.Champagne, V.G.Harris, S.Corrsin (1970) Experiments on nearly homogeneous turbulent shear flow; J. Fluid Mech., vol.41 pp.81-139

[18] V.G.Harris, J.A.H.Graham S.Corrsin (1977) Further experiments in nearly homogeneous turbulent shear flow; J. Fluid Mech., vol.81 pp.657-687

[19] C.W.Mastin, J.F.Thompson (1978) Transformation of three dimensional regions onto rectangular regions by elliptic systems; Number. Math., vol.29 pp.397-407

[20] B.P.Leonard (1979) A stable and accurate convective modelling procedure based on quadratic upstream interpolation; Comp. Meths. Appl. Mech. Eng., vol.19 pp.59-98

[21] B.E.Launder, S-P.Li (1993) On the prediction of the flow over riblets via 2nd–moment closure; *Near-Wall Turbulent Flows* 1993 pp.739–748

[22] I.Nakamura, M.Miyata, J.Matsuda, Y.Furuya (1993) The secondary flow and the turbulent structure in the turbulent boundary layer along a streamwise rectangular bar on a flat plate; Trans. Jpn. Soc. Mech. Eng., vol.46 pp.239–246 (in Japanese)